Numerical study of drop shape effects in binary drop film interactions for different density ratios

J. Steigerwald*[1], A. Geppert[1], B. Weigand[1]
[1]Institute of Aerospace Thermodynamics (ITLR), University of Stuttgart, Germany
*Corresponding author email: jonas.steigerwald@itlr.uni-stuttgart.de

Abstract

When a drop impacts onto a liquid film the outcome can differ very much and is in general difficult to parameterize due to the many influencing parameters. A parameter often idealized when studying drop film interactions is the shape of the impacting drop. Whereas for one-component interactions its influence on the impact outcome is known to some extent, its influence is still unknown for binary interactions, where the liquids of the drop and film differ. For this reason, we investigate numerically possible drop shape effects for binary drop film interactions in this study. The simulations are performed with the multiphase flow solver Free Surface 3D (FS3D), which is based on the volume-of-fluid (VOF) method. Two binary drop film interactions are simulated, for which the liquids of the drop and the film, exhibiting a density difference of around 14%, are permuted. Both impact scenarios are simulated three times with various initialized drop shapes and the results are compared with experimental data. The study shows that the drop shape can have a strong effect on the resulting crown morphology in binary drop film interactions in case the density of the drop liquid is higher than the density of the film liquid.

Keywords

DNS, VOF, Binary drop impact, Density ratio, Drop shape

Introduction

The interaction of a drop with a liquid film is a fundamental process that determines many natural as well as technical processes [1]. In order to gain a fundamental understanding of the highly different impact outcomes of such interactions, experimental and numerical studies have already been conducted for decades, due to the many influencing parameters [1]. In experimental investigations of drop film interactions, the diameter of the drops lies typically in the millimeter regime [1]. Since the drop size is larger than the capillary length, the drop shape is prone to deformations during the free fall in the experiments [2]. In many real applications, the diameter is one or even two orders of magnitude smaller, like in inkjet-printers or in combustion engines with fuel injection [1], so that the assumption of perfect spherical drops appears reasonable. In the latter application, however, the conditions of the surrounding fluid can be very different than in the experiments (higher density), so that drops can still deform.

In general, the influence of the drop shape on the impact outcome is assumed to be negligible. Investigations on the influence of the drop shape on the impact outcome are mainly limited to numerical studies because the drop can hardly be forced into a desired static shape just before the impact in the experiment. However, even numerical investigations about the influence of the pre-impact drop shape on the splashing morphology are quite rare in the literature, see e.g. [3-5]. Furthermore, the liquids of the drop and the film or pool, respectively, are always identical in these studies. In many technical systems like for example in fuel injection systems, however, binary drop film interactions take place where liquids of the drop and the film differ. The influence of the various drop shapes on the impact outcome in such binary interactions is still unknown and was, to the best of our knowledge and in contrast to

unary drop film interactions, never investigated before. For this reason, we numerically investigate in this study possible drop shape effects for two selected binary drop film interactions by using the in-house multiphase flow solver Free Surface 3D (FS3D). Both interactions are simulated three times with differently initialized drop shapes. Since we assume that the density ratio between drop and film liquid could play an important role, we choose reference cases with a density difference of both liquids of around 14%. On the one hand, the results shall help to quantify possible deviations from the assumption of a perfect spherical drop. On the other hand, a comparison of the obtained numerical results with experimental data serves as additional code validation.

Numerical Method and Computational Setup

Numerical Method

The simulations in this study were performed by using FS3D, which is capable of simulating two-phase flows with two different liquids. FS3D solves the governing conservation equations for mass and momentum

$$\partial_t \rho + \nabla \cdot (\rho \mathbf{u}) = 0, \tag{1a}$$

$$\partial_t (\rho \mathbf{u}) + \nabla \cdot (\rho \mathbf{u} \otimes \mathbf{u}) = \nabla \cdot [\mathbf{S} - \mathbf{I}p] + \rho \mathbf{g} + \mathbf{f}_\gamma \tag{1b}$$

using finite volumes (FV), where ρ denotes the density, p the pressure, $\mathbf{u}$ the velocity vector, $\mathbf{g}$ the acceleration of gravity, $\mathbf{I}$ the identity matrix, and $\mathbf{S}$ the shear stress tensor. The term $\mathbf{f}_\gamma$ incorporates the surface tension force as a volume force at the interface between the liquid and the gaseous phase. In order to distinguish between both phases, FS3D uses the volume-of-fluid (VOF) method by Hirt and Nichols [6], in which an indicator function is used to introduce the scalar field

$$f(\mathbf{x}, t) = \begin{cases} 0 & \text{outside the liquid phase,} \\ ]0,1[& \text{in interface cells,} \\ 1 & \text{inside the liquid phase,} \end{cases} \tag{2}$$

representing the liquid volume fraction in each control volume, where $\mathbf{x}$ denotes the Cartesian coordinate vector**.** For the treatment of distinguishable liquids, additional intrinsic averaged VOF variables $\psi_i = V_i / V_l$ are introduced in FS3D, which represent the volume fractions of each species i in the liquid volume in a control volume V_l. Between the different species, a linear mixing behavior without volume expansion is assumed. For the advection of the liquid phase, the additional transport equation

$$\partial_t f + \nabla \cdot (f \mathbf{u}) = 0, \tag{3}$$

is solved as described by Rider and Kothe [7]. The VOF-fluxes are thus calculated geometrically by means of the piece-wise linear interface calculation (PLIC) method to maintain a sharp interface during the advection. To guarantee volume conservation during the advection, the dilatation term which occurs due to the directional splitting of equation (3) is treated as suggested by Weymouth and Yue [8]. The volume fractions of each species are advected analogously with further transport equations

$$\partial_t (f \psi_i) + \nabla \cdot (f \psi_i \mathbf{u}) = 0, \tag{4}$$

which are solved simultaneously and in a closely coupled way to equation (3). As the problem of investigation in this study is strongly convection-dominated, molecular diffusion between species can be neglected, leading to the zero right-hand side of equation (4). For a correct behavior of the interface with respect to surface tension, the conservative continuum surface stress (CSS) model by Lafaurie et al. [9] is used in this study.

The conservation equations are solved in the one-field formulation, so that all fluids are treated as a single fluid with varying physical properties that depend on f, ψ_i, and the properties of the pure gaseous and liquid fluids. Therefore, a local physical property φ (e.g. the density) within the flow field is calculated with

$$\varphi(\mathbf{x},t) = \varphi_l f(\mathbf{x},t) + \varphi_g\big(1 - f(\mathbf{x},t)\big) \quad \text{with} \quad \varphi_l = \varphi_l(\psi_D, \psi_F), \tag{5}$$

where the subscripts l and g denote the liquid and the gaseous phase and the subscripts D and F denote the liquid of the drop and film, respectively. The liquid mixture density is calculated as weighted arithmetic mean ensuring mass conservation since no excess volume is generated during mixing. The liquid mixture viscosity is calculated with the volume fraction based viscosity mixture model for binary liquid mixtures by Dey and Biswas [10]. Even though FS3D is capable of simulating soluto-capillary driven flows, the surface tension is set to an averaged value of $\bar{\sigma} = (\sigma_D + \sigma_F)/2$ in this study for reasons of simplicity. Furthermore, FS3D is parallelized using MPI as well as OpenMP allowing simulations on high performance computers such as the HPE Apollo (Hawk) at the supercomputing center (HLRS) in Stuttgart, where the simulations presented in this paper were calculated.

Computational Setup

The computational domain is almost identical to the one used by Kaufmann et al. [11] and is therefore only briefly described here. Due to the symmetry of the problem, only a quarter of the drop impact is simulated. A drop with diameter *D* is initialized in a distance of 2*D* above a liquid film of thickness *h* in a cubic domain with dimensions 7*D* in each direction. The drop exhibits an initial velocity *U* towards the film. The computational domain is discretized with a Cartesian grid consisting of 1024^3 cells. The region where the impact takes place has the dimensions $2D^3$ and is discretized with an equidistant grid with 512^3 cells. The drop is thus resolved with 256 cells/*D*. Outside this region a stretched cell arrangement is used. At the boundaries of the domain three different types of boundary conditions are applied: A no-slip boundary condition at the bottom, two symmetry boundary conditions in the *x*–*z*–plane and in the *y*–*z*–plane, and homogeneous Neumann boundary conditions at all remaining sides.

Two different impact scenarios are simulated, whose parameters are summarized in Table 1. The parameters originate from experiments, whose setup and operation are described in detail by Geppert [12]. The used liquids are n-hexadecane $C_{16}H_{32}$ (long-chain alkane) and Hyspin AWS 10 (hydraulic oil) and are permuted in both investigated cases. Their physical properties can be found in [12] as well. The non-dimensional parameters in Table 1 are the non-dimensional film thickness $\delta = h/D$, the Weber number of the drop $We = (\rho_D U^2 D)/\bar{\sigma}$, the averaged Ohnesorge number $\overline{Oh} = \bar{\mu}/\sqrt{\overline{\rho\sigma}D}$, the density ratio $\chi = \rho_D/\rho_F$, the viscosity ratio $\lambda = \mu_D/\mu_F$, and the surface tension ratio $\gamma = \sigma_D/\sigma_F$. Furthermore, the gravitational acceleration is $g =$ 9.81 m/s² and the properties of the ambient air are $\rho_g =$ 1.204 kg/m³ and $\mu_g =$ 1.813 × 10^{-5} Pa s. All relevant dimensional parameters are visualized in Figure 1.

Both cases 1 and 2 (see Table 1) are simulated three times, whereas the drop in the computational domain is initialized successively with three different shapes: As a sphere with diameter D, as an oblate spheroid and as an asymmetrical oblate spheroid. The sphere dia-

Table 1 - Overview on numerically investigated drop film interactions with corresponding parameters.

Case	Drop liquid	Film liquid	D [mm]	h [mm]	U [m/s]	δ [-]	We [-]	$\overline{Oh}$ [-]	χ [-]	λ [-]	γ [-]
1	Hexadecane	Hyspin	2.440	1.000	4.48	0.41	1346	0.0404	0.880	0.218	1
2	Hyspin	Hexadecane	2.406	0.933	4.49	0.37	1514	0.0407	1.136	4.580	1

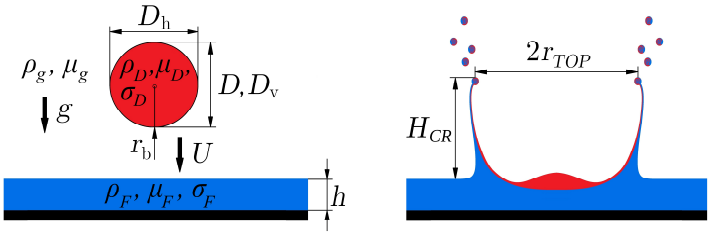

Figure 1. Schematic setup with relevant parameters (left) and crown parameters (right).

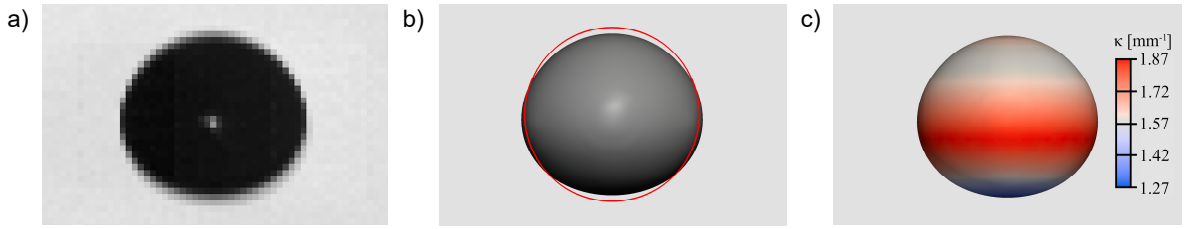

Figure 2. a) Drop before the impact in the experiment (case 2) with $\alpha = 0.897$; b) iso-surface $(f = 0.5)$ of the reconstructed asymmetric oblate spheroid in the simulation in comparison to the shape of a sphere (red circle); c) iso-surface mapped with the local curvature κ for estimating the effective drop radius r_b at the impact.

meter is obtained by evaluating the projected area A_{proj} of the drop from the side view from Figure 2a, such that $D = \sqrt{4A_{proj}/\pi}$ [12]. The oblate spheroid is characterized by the aspect ratio $\alpha = D_v/D_h$, where D_v and D_h are the vertical and horizontal diameters, respectively. In this study $\alpha = 0.897$ as evaluated from the experiment [12]. Since the kinetic energy of the impacting drop has to be the same regardless of the drop shape, D_v and D_h can be calculated by assuming equal drop volumes V. The asymmetric oblate spheroid (see Figure 2b) is initialized with a formula by Wang [13]. A two-dimensional axial cross-section of the asymmetric shape is described as a modified ellipse by $x = \pm a[1 - (z^2/C^2)]^{1/2} \cos^{-1}(z/(\theta C))$, where a, $C = D_v/2$, and θ are geometrical parameters. The three-dimensional drop shape is obtained by rotating the resulting cross-section around the z-axis afterwards, leading to the volume of $V_{AS} \approx 3.292\pi a^2 C$ for the presented cases (see [13] for details).

Furthermore, different drop shapes result in different bottom radii r_b of the drops and, therefore, in different effective Weber numbers (We, We_S, We_{AS}) at the impact. For the oblate spheroid, this Weber number is given by $We_S = \rho_D D_h U^2/(\alpha\bar{\sigma})$ with $r_b = D_h/(2\alpha)$ and is, therefore, 15.6% larger than We for the sphere. For the asymmetric oblate spheroid, r_b is evaluated directly from the initialized shape via the curvature at the bottom $\kappa_b = 2/r_b$ (see Figure 2c), which yields $We_{AS} = 4\rho_D U^2/(\kappa_b\bar{\sigma})$. This leads to an increase in the effective Weber number of 30.6% in comparison to the one of the sphere. All relevant parameters of the used drop shapes are listed in Table 2 and are visualized in parts in Figure 1.

Table 2 - Parameters of initialized drop shapes of the numerically investigated drop film interactions.

Case	Sphere		Oblate spheroid				Asymmetric oblate spheroid			
	D [mm]	We [-]	$\alpha = D_v/D_h$ [-]	D_v [mm]	D_h [mm]	We_S [-]	a [mm]	θ [-]	κ_b [1/mm]	We_{AS} [-]
1	2.440	1346	0.897	2.269	2.530	1556	0.8051	10	1.255	1758
2	2.406	1514	0.897	2.238	2.495	1750	0.7939	10	1.273	1978

Results and Discussion

Figure 3 shows side views of the splashing morphology for all performed simulations at the non-dimensional time $\bar{t} = tU/D = 0.5$. The first row (Figure 3a-c) shows the results of case 1 and the second row (Figure 3d-f) of case 2, whereas columns 1 to 3 correspond to the

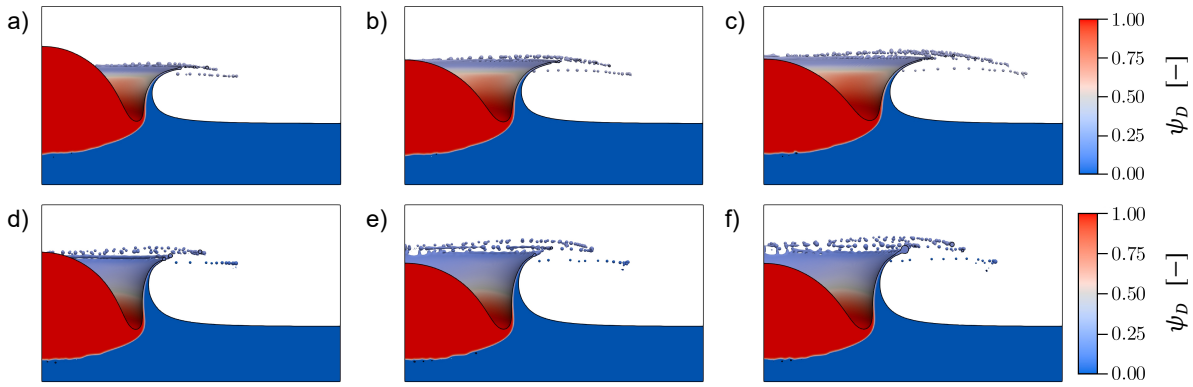

Figure 3. Side view of the splashing morphology with internal distribution of the drop species ψ_D for case 1 (a-c) and case 2 (d-f) at $\bar{t} = tU/D = 0.5$ for different initialized drop shapes: Sphere (left column), oblate spheroid (middle column), and asymmetric oblate spheroid (right column).

different initialized drop shapes. Each figure shows also the distribution of the drop species ψ_D at the crown wall and inside the liquid phase. As can be seen, an increase of the effective Weber number promotes prompt splashing in the simulation in both cases. The increase of r_b leads to a higher velocity at the neck between the drop and the film at very early times of the impact because $v_{neck} \approx \sqrt{r_\mathrm{b}}$ [2]. Thus, the ejection velocity of the secondary droplets is directly influenced by the drop shape at this stage of the impact. This increase of the ejection velocity is, however, more pronounced in case 1 which can be explained by the density ratio of the liquids χ. Semenov et al. [14] showed analytically, that during an impact between two non-isodense fluids exhibiting the same pre-impact geometry, the resulting flow points into the direction of the heavier fluid in the co-moving frame of the occurring stagnation point between both fluids. Since the geometrical setup is identical in both cases, the crown has therefore to be flatter in case 1 than in case 2, which is indeed the case. The resulting stronger thinning of the crown wall in case 1 due to the stronger radial fluid flow leads thus to an enhanced prompt splashing. The observed small differences caused by the various shapes of the impacting drop also influence the development of the crown in the further course of the drop film interaction. This can be seen in Figure 4, which shows contour slices through the developing crowns for case 1 (Figure 4a) and case 2 (Figure 4b) for four different times. For case 1, the differences

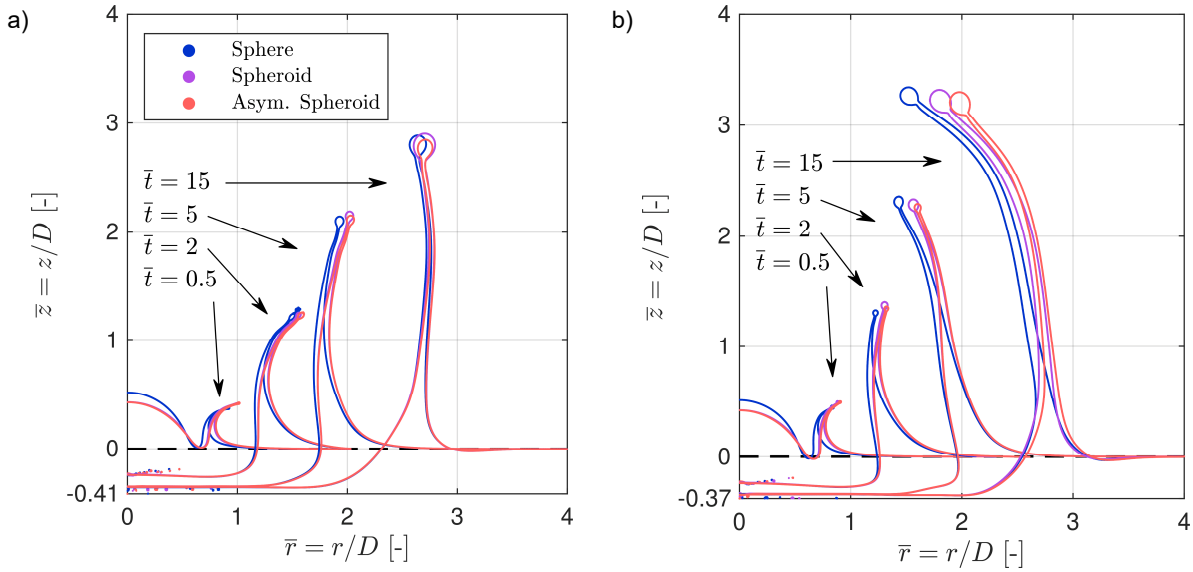

Figure 4. Slices through the developing crowns for case 1 (a) and (b) at four different times for the three different drop shape initializations.

from the early stages of the impact continue to exist in the further course but do not seem to affect any crown characteristic at later times. At $\bar{t} = 15$, the contour slices of the three cylindrical crowns lie almost on top of each other. In contrast to that, the initial differences in case 2 further increase. An increase of the effective Weber number leads to a reduction of the crown angle and to a significant weaker constriction of the crown rim.

In order to quantify the differences between the resulting crown shapes, the temporal development of the crown height $\bar{H}_{CR} = H_{CR}/D$ and the crown top radius $\bar{r}_{TOP} = r_{TOP}/D$ was evaluated. The latter was also compared to experimental data till $\bar{t} = 15$, which is shown in Figure 5. A detailed description how the crown parameters are evaluated from the simulation can be found in Kaufmann et al. [11]. For both cases 1 and 2, $\bar{H}_{CR}$ evolve almost unaffected by the initial drop shape (see Figure 4), which is in accordance with the results of Shetabivash et al. [4] for the given α. For the temporal development of $\bar{r}_{TOP}$ the situation is different. In case 1, drop shape effects in the simulations are negligible. The small differences between the simulations and the experiment between $\bar{t} = 1$ and $\bar{t} = 5$ can be explained by a premature disintegration in the simulation due to the coarse grid resolution and the different evaluation methodologies for the simulation and experiment. The overall agreement between experiment and simulation can be considered as very good, as can also be seen in Figure 6a. Figure 6 shows the comparison of the impact morphology for both cases 1 (Figure 6a) and 2 (Figure 6b) between the experiment and the numerical simulation with the drop initialization as asymmetric oblate spheroid. The colors in the numerical results correspond again to the drop liquid (red) and the film liquid (blue) like in Figure 3. In contrast to case 1, the temporal development of $\bar{r}_{TOP}$ of case 2 (Figure 5b) shows significant differences in dependence on the initialized drop shape. When the drop is initialized as a perfect sphere, $\bar{r}_{TOP}$ remains constant for $\bar{t} > 5$, whereas for both spheroidal drop shapes $\bar{r}_{TOP}$ further increases with time. At $\bar{t} = 15$, $\bar{r}_{TOP}$ is ≈18% larger when the drop is initialized as an oblate spheroid and 30% larger when it is initialized as observed in the experiment (see Figure 2a). An increase of r_b will, therefore, influence the thickness of the crown wall, the shape of the crown rim and, most importantly, the resulting drop size distribution. In comparison to the experiment, the numerically obtained $\bar{r}_{TOP}$ still underestimates the experimental one. However, due to the more realistic drop shape initialization it shows now almost the same growth rate as in the experiment. The differences between the simulation and the experiment can again be explained in multiple ways. Besides the different evaluation methodologies, the premature disintegration of the crown top in the simulation and the accompanied generation of secondary droplets affects the radius. In the experiment, the top of the crown is so strongly curved that the position of the generated droplets is lower than the actual crown top (see Figure 6b at $\bar{t} = 2.52$). The retraction of the rim occurs therefore more in the vertical direction than in the

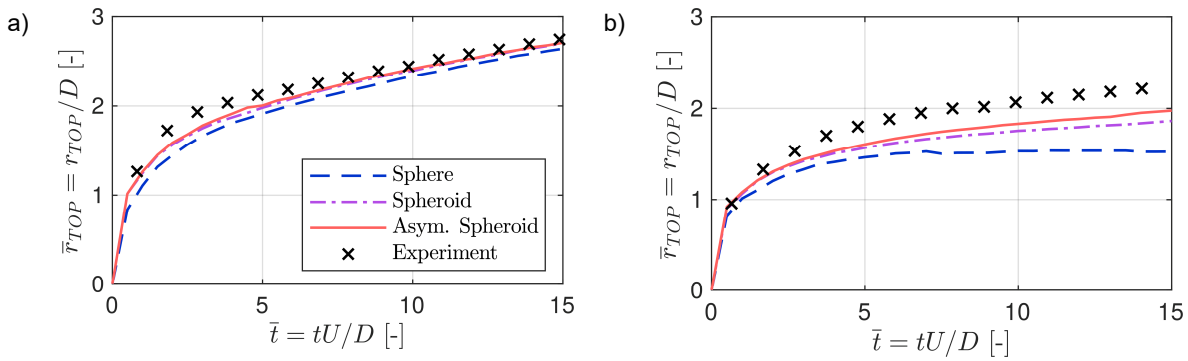

Figure 5. Temporal evolution of the non-dimensional crown top radius $\bar{r}_{TOP}$ for (a) case 1 and for (b) case 2 for different initialized drop shapes.

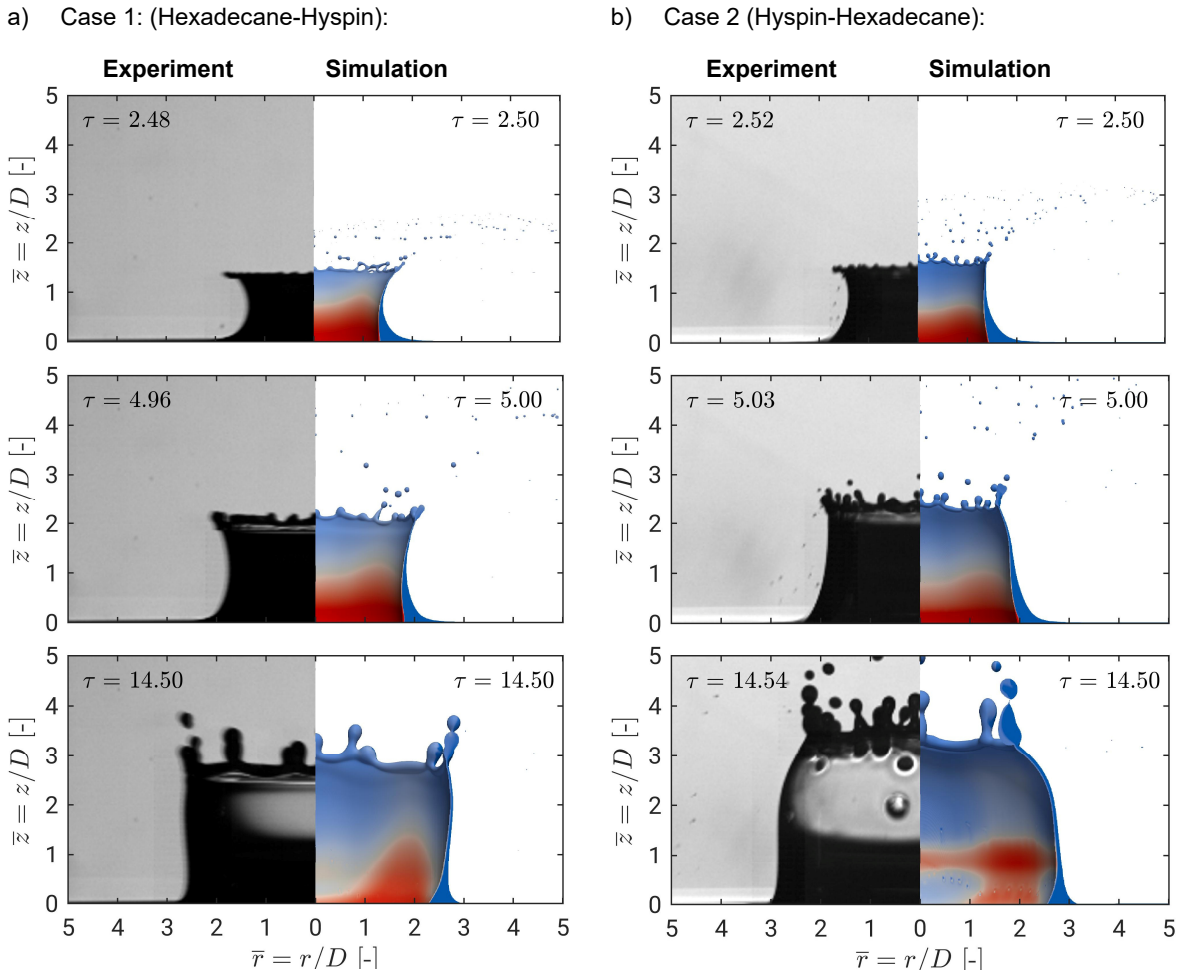

Figure 6. Comparison of experimental and numerical splashing morphology of binary drop film interactions for several time steps; a) Case 1; b) Case 2 with a drop initialization as asymmetric oblate spheroid after Wang [13]. The different gray levels in pictures of the experiments are caused by the setting of illumination, whereas the colors in the simulations show the species distribution at the crown wall (red: Drop liquid; blue: Film liquid).

horizontal direction. In contrast to that, the direction of the retraction in the simulation is almost horizontal (see Figure 3d-f) in the co-moving frame of the crown top. The radial position of the crown top is thus more affected in the simulation than in the experiment. Another important uncertainty is the drop shape because a further increase of r_b could probably lead to a temporal evolution of $\bar{r}_{TOP}$ that nestles even closer to the experimental one. Nevertheless, the overall agreement of the impact morphology can be considered to be good, even though small differences of the crown top radius are visible due to the reasons mentioned above (see Figure 6b).

The results above show, that the shape of the impacting drop can have a significant influence on the overall splashing morphology and on the crown top radius, especially when the density of the drop liquid is higher than the film liquid. Only due to the initialization of the drop as a realistic asymmetric oblate spheroid (see Figure 2b) the crown shape of case 2 could be numerically reproduced (see Figure 6b). In the opinion of the authors, the main reason for this different behaviour of both cases is the different momentum transfer between both liquids during the impact due to the different density ratio χ. The authors conclude, that the resulting crowns are probably more prone to drop shape effects for $\chi > 1$ than for $\chi < 1$ for the same film thickness δ. An exact explanation for the observed different behavior of both cases can, however, not be given at this point, but is a topic of current research.

Summary and Conclusions

In this study, we numerically investigated the influence of various drop shapes on the resulting crown morphology in binary drop film interactions by using FS3D. Two impact scenarios were investigated, for which the liquids of drop and film were permuted. For both cases, the drop shape, which is mostly been assumed to be perfect spherical in the literature, was initialized as a sphere, as an oblate spheroid, and as asymmetric oblate spheroid in the computational domain. For the initialization of the latter, formulae by Wang [13] were used.

In both cases, the increase of the effective Weber number ($We < We_{\mathrm{S}} < We_{\mathrm{AS}}$) at the impact leads to an enhanced prompt splashing in the simulation. However, this effect is more pronounced for the case with the smaller χ due to the resulting flatter crown. The crown height $\overline{H}_{CR}$ is not influenced by the drop shape in both cases. In contrast to that, the crown top radius $\bar{r}_{TOP}$ showed a significant increase with an increasing effective We for $\chi > 1$ (up to 30%), whereas for $\chi < 1$ the difference was negligible. A comparison between the obtained numerical results and experiments showed good agreement, however, only when the drop shape was initialized as observed in the experiment for the case with $\chi > 1$. This study shows that the assumption of a perfect spherical impacting drop might be sufficient for many cases but can also lead to non-negligible deviations from the experimental results. Such deviations can – in the worst case scenario – unnecessarily question the accuracy of the used numerical method if the investigators are not aware of the effect that a non-spherical drop shape can have on the impact morphology. The authors therefore suggest, that in the future for comparisons with experiments the shape of the impacting drop should always be taken correctly into account.

Acknowledgements

The authors kindly acknowledge the financial support of the Deutsche Forschungsgemeinschaft (DFG) through the project WE2549/35-1 and within the international research training group DROPIT (GRK2160; 270852890). In addition, the authors kindly acknowledge the High Performance Computing Center Stuttgart (HLRS) for support and supply of computational time on the HPE Apollo system “Hawk” under Grant No. FS3D/11142.

References

[1] Liang, G. and Mudawar, I., 2016, Int J Heat Mass Tran, 101, pp. 577-599.
[2] Li, E. Q., Thoraval, M.-J., Marston, J. O., and Thoroddsen, S. T., 2018, J Fluid Mech, 848, pp. 821-835.
[3] Dinc, M. and Gray, D. D., 2013, International Journal of Mechanics, 7, pp. 26-36.
[4] Shetabivash, H., Ommi, F., and Heidarinejad, G., 2014, Phys Fluids, 26, 012102.
[5] Thoraval, M.-J., Li, Y., and Thoroddsen, S. T., 2016, Phys Rev E, 93, 033128.
[6] Hirt, C. W. and Nichols, B. D., 1981, J Comput Phys, 39(1), pp. 201-225.
[7] Rider, W. J. and Kothe, D. B., 1998, J Comput Phys, 141(2), pp. 112-152.
[8] Weymouth, G. D. and Yue, D. K.-P., 2010, J Comput Phys, 229(8), pp. 2853-2865.
[9] Lafaurie, B., Nardone, C., Scardovelli, R., Zaleski, S., and Zanetti, G., 1994, J Comput Phys, 113(1), pp. 137-147.
[10] Dey, R. and Biswas, P., 2018, J Mol Liq, 265(1), pp. 356-360.
[11] Kaufmann, J., Geppert, A., Ertl, M., Bernard, R., Vaikuntanathan, V., Lamanna, G., Weigand, B., July 22 – 26, 2018, ICLASS, Chicago, Illinois, USA.
[12] Geppert, A. K., 2019, Ph. D. thesis, University of Stuttgart.
[13] Wang, P.-K., 1982, J Atmos Sci, 39(11), pp. 2615-2622.
[14] Semenov, Y. A., Wu, G. X., and Korobkin, A. A., 2015, J Fluid Mech, 766, pp. 5-27.